Formation of protein-mediated bilayer tubes is governed by a snapthrough transition

A. Mahapatra and P. Rangamani*

Department of Mechanical and Aerospace Engineering,
University of California San Diego, La Jolla CA 92093.
*To whom correspondence must be addressed: prangamani@ucsd.edu

Abstract

Plasma membrane tubes are ubiquitous in cellular membranes and in the membranes of intracellular organelles. They play crucial roles in trafficking, ion transport, and cellular motility. These tubes can be formed due to localized forces acting on the membrane or by the curvature induced by membrane-bound proteins. Here, we present a mathematical framework to model cylindrical tubular protrusions formed by proteins that induce anisotropic spontaneous curvature. Our analysis revealed that the tube radius depends on an effective tension that includes contributions from the bare membrane tension and the protein-induced curvature. We also found that the length of the tube undergoes an abrupt transition from a short, dome-shaped membrane to a long cylinder and this transition is characteristic of a snapthrough instability. Finally, we show that the snapthrough instability depends on the different parameters including coat area, bending modulus, and extent of protein-induced curvature. Our findings have implications for tube formation due to BAR-domain proteins in processes such as endocytosis, t-tubule formation in myocytes, and cristae formation in mitochondria.

Keywords— membranes tubes, snapthrough, BAR-domain proteins

1 Introduction

The generation of membrane curvature is a ubiquitous phenomenon in cells, both at the plasma membrane and at organelle membranes (*1*). These curved structures can be broadly classified into buds, pearled structures, and tubes (*2*, *3*). Specifically, the formation of tubes on membranes is attributed to either the interaction of cellular membranes with proteins that induce curvature or to forces exerted on the membrane by cytoskeletal assembly and motor proteins, among other mechanisms. Force-mediated membrane tubulation is quite well-studied and the relationship between the applied force and membrane properties is well understood (*4*, *5*). However, there are many situations in cells where cylindrical tubes are formed due to curvature-inducing proteins alone without any apparent force mechanisms (*6*, *7*). In this study, we focus on such protein-mediated tube formation.

Protein-mediated tubes are essential components in numerous biophysical processes in a cell (Figure 1a). For example, in yeast, BAR(Bin/Amphiphysin/Rvs)-domain proteins play an important role in the elongated endocytic invaginations (*8*) and these proteins are known to dimerize and form curved structures. BAR-domain proteins such as BIN1 play an important role in the formation and maintenance of t-tubules in myocytes; these tubular structures are critical for excitation-contraction coupling (*6*, *9*). Protein-decorated tubes are also important in intracellular organelles including the ER-Golgi complex (*10*, *11*) and cristae in a mitochondria (*7*). Experiments using BAR-domain proteins can generate tubular protrusions formed from liposomes *in vitro* (*12–15*). Stachowiak *et al.* (*16*) showed that protein crowding on giant unilamellar vesicles can cause tubulation, when a high density of proteins are attached.

From a theoretical standpoint, the mechanism of tube formation has been studied quite extensively using continuum mechanics and molecular dynamics simulations (*17–19*). Our focus here is on continuum models where the Helfrich energy (*20*) is used to capture the bending energy of the membrane and a spontaneous curvature is used to capture asymmetries between the two leaflets. When an isotropic spontaneous curvature is used in the Helfrich energy, spheres and pearls emerge as energy-minimizing shapes because the minimum energy state of these geometries is such that both principal curvatures have the same value (*21*, *22*). Our geometry of interest is a complete cylindrical tube, defined here as a cylindrical membrane with a hemispherical cap and our goal is to use a single set of equations that will allow us to obtain such shapes numerically. However, the use of the classical Helfrich energy with an isotropic spontaneous curvature term will not admit solutions that will give rise to cylindrical tubes with a hemispherical cap. To obtain a cylinder, we need a formulation that accounts for one principal curvature to capture the cylinder's radius and the other principal curvature to equal zero (Figure 1b) along the tube. This can be done by recasting the Helfrich energy in terms of the mean curvature and the curvature deviator (*23*, *24*). Such models have been proposed and simulations have been used to explore tubulation (*25*, *26*) and the impact of BAR-domain proteins on endocytosis (*27*).

In this work, we conducted a detailed mechanical analysis of tube formation due to membrane-bound proteins that induce anisotropic curvature using the curvature deviator version of the Helfrich model. We found that the formation of membrane tubules due to anisotropic curvature is governed by a snapthrough instability that depends on the membrane tension and the bending modulus. We also establish scaling relationships between membrane tension, extent of anisotropic curvature, and the bending modulus and the tube dimensions. Finally, we predict how the snapthrough instability and the bending energy landscape vary with different membrane parameters.

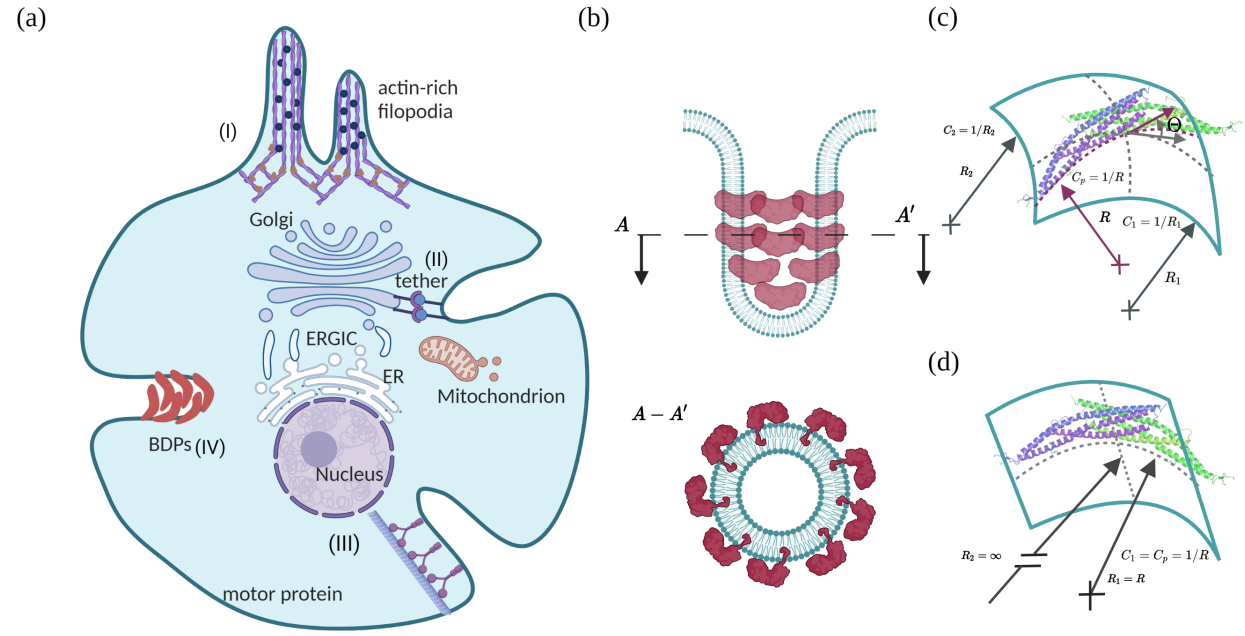

Figure 1: Schematic of protein-induced tube formation on cellular membranes. a) Mechanisms of tube formation in cellular membranes. (I) Tubes can be formed due to forces exerted on the membrane by the cytoskeleton, e.g. filopodial protrusion by actin filaments, (II) localized forces such as tethers and motors (III) can also lead to the formation of tubes. Tubules can also be formed by curvature-inducing proteins, such as BAR-domain proteins (BDPs) (IV). BDPs are know to form cylindrical tubules by inducing anisotropic curvature on the lipid bilayer. (b) Schematic depicting proteins that have anisotropic curvatures assembled on the cylindrical portion of a membrane tube. The top subplot presents a side-view of the tube, and the bottom subplot shows the top view of the tube with BDPs. (c) The structure of a typical BAR-domain protein dimer (*28*) induces two different curvatures in the parallel and perpendicular direction to enable a cylindrical deformation. (d) The particular case of BAR-domain dimer orientation causes curvature generation in one principal direction leading to a tubular protrusion.

2 Model development

From a geometric perspective, a membrane can be described from the mean (H) and deviatoric (D) curvature, as given by

$$H = \frac{c_1 + c_2}{2}, \quad D = \frac{c_1 - c_2}{2}, \tag{1}$$

where c_1 and c_2 are the principal curvatures of the surface. Specific combinations of these curvatures define characteristic surfaces such as spherical buds, tubes, and catenoids. BAR-domain proteins (BDPs) are a classic example of curvature-inducing proteins that result in membrane tubes. This family of proteins can be treated as one-dimensional curved proteins (*28*) that induce anisotropic curvature to the membrane (Figure 1c,d, also see (Figure S1)) (*23*, *26*, *34*). If C_1 and C_2 are the curvatures induced by the proteins in the two principal directions, the spontaneous mean (C_0) and deviatoric (D_0) curvatures are given by

$$C_0 = \frac{C_1 + C_2}{2}, D_0 = \frac{C_1 - C_2}{2}. \tag{2}$$

Note that the principal components of the induced curvatures, C_1 and C_2, will depend on the value of curvature C_p of the BAR-domain proteins and the orientation angle Θ (Figure 1c). For such orientation, the spontaneous mean (C_0) and deviatoric curvature (D_0) relate to the curvature of the proteins (C_p) and their orientation angle Θ with the following

Table 1: Notation and list of symbols

Notation	Description	Unit
W	Free energy density of the membrane	pN/nm
κ	Bending modulus of the membrane	pN · nm
κ_d	Deviatoric modulus of the membrane	pN · nm
κ_p	Bending modulus BAR-domain protein's coat	pN · nm
$\boldsymbol{n}$	Surface normal	1
$\boldsymbol{\zeta}$	Orientation vector of proteins	1
$\boldsymbol{\mu}$	Binormal vector of protein $\boldsymbol{\mu} = \boldsymbol{n} \times \boldsymbol{\zeta}$ (see Figure S1)	1
$a_{\alpha\beta}, a^{\alpha\beta}$	Metric tensor and its contravariant	–
$b_{\alpha\beta}, b^{\alpha\beta}$	Curvature tensor and its contravariant	–
s	Arclength along the membrane	nm
ψ	Angle made by surface tangent with the horizontal direction	1
C_p	Curvature of the BAR-domain protein rods	nm^{-1}
C_1, C_2	Protein-induced principal curvatures	nm^{-1}
C_{eff}	Effective spontaneous curvature generated by proteins on membrane	nm^{-1}
c_1, c_2	Principal curvatures of the membrane	nm^{-1}
H	Mean curvature	nm^{-1}
D	Deviatoric curvature	nm^{-1}
C_0	Spontaneous mean curvature	nm^{-1}
D_0	Spontaneous deviatoric curvature	nm^{-1}
$C_{0,eff}$	Effective spontaneous mean curvature	nm^{-1}
$D_{0,eff}$	Effective spontaneous deviatoric curvature	nm^{-1}
$\boldsymbol{T}$	Surface traction	pN/nm
p	Normal pressure acting on the membrane	pN/nm^2
λ	Membrane tension	pN/nm
W	Bending energy per unit area of the membrane	pN/nm
E	Bending energy of the membrane	pN · nm
$\mathcal{F}$	Bending energy of BAR-domain protein	pN

Table 2: List of parameters

Notation	Description	Range
C_0	Spontaneous mean curvature	0.01–0.02 nm^{-1} (*18*)
D_0	Spontaneous deviatoric curvature	0.01–0.02 nm^{-1} (*18*)
$\kappa(=\kappa_d)$	Bending modulus of the membrane	21–336 pN · nm $(5-80$ k$_B$T$)$ (*29*, *30*)
λ_0	Membrane tension at the boundary	0.001–0.1 pN/nm (*31*, *32*)
a_{coat}	Coat area of the protein	2.5×10^4–5×10^4 nm^2 (*33*)

relationship (*25*, *35*, *36*)

$$C_p = \left(\frac{C_1 + C_2}{2}\right) + \left(\frac{C_1 - C_2}{2}\right)\cos(2\Theta) = C_0 + D_0\cos(2\Theta). \tag{3}$$

In the example shown in Figure 1d, BDPs orient circumferentially along a cylindrical membrane ($C_2 = 0$) with orientation angle $\Theta = 0$. In this case, minimization of the free energy of orientation gives rise to spontaneous mean and deviatoric curvatures is given by

$$C_0 = \frac{C_p}{2} \quad \text{and} \quad D_0 = \frac{C_p}{2}. \tag{4}$$

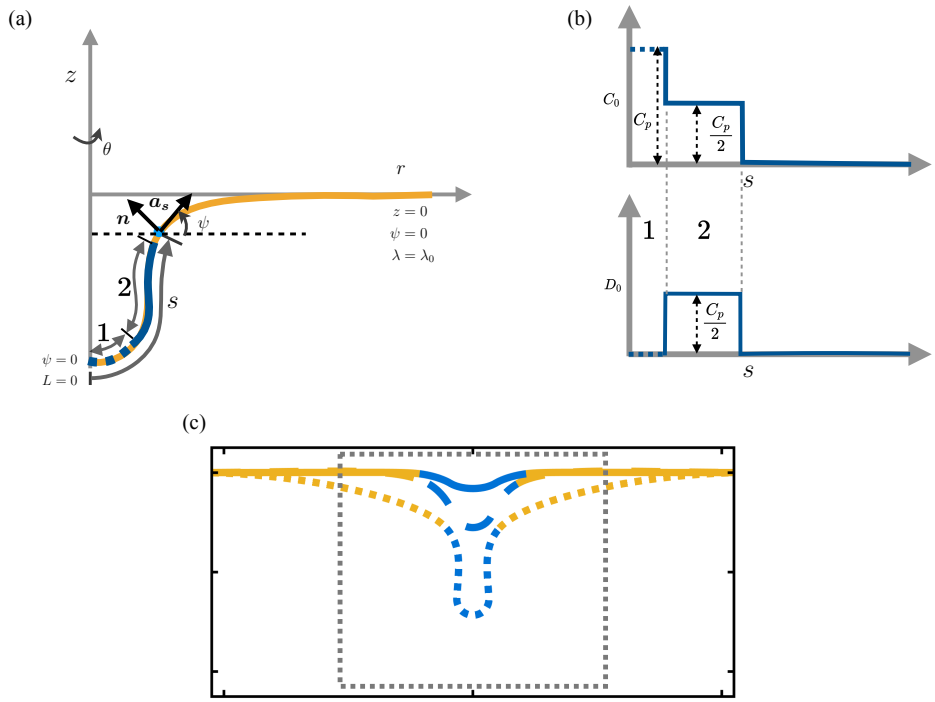

Figure 2: Membrane representation in axisymmetry with protein distribution area and boundary conditions. (a) Computational domain showing the axisymmetric coordinates, location of the protein coat, and boundary conditions. (b) Input distribution of spontaneous mean and deviatoric curvatures on the membrane along its arclength. (c) Representative deformed membrane configuration; the dashed lines show the region in the $r - z$ plane we show in the subsequent figures.

2.1 Assumptions

We assumed that membrane thickness and change in thickness are negligible compared to bending, and thus the Helfrich description is valid in this case. The membrane is elastic in bending, and the bending rigidity is assumed to be uniform across the solution domain (Figure 2a). We also assumed that the membrane is incompressible and in mechanical equilibrium. For computational simplicity, we assumed that the tubule is rotationally symmetric. We do not consider the molecular details of the protein-induced curvature but rather use spatial distributions of C_0 and D_0 as inputs to the model. We restricted the orientation angle $\Theta = 0$ to minimize the number of free input parameters (see Equation (3)) and assume that the proteins that induce curvature are rigid and non-deformable.

To capture the hemispherical cap and the cylindrial tube regions of the membrane, we assumed that the spontaneous mean and deviatoric curvature induced by membrane-bound BDPs are divided into two regions (see Figure 2),
i. at the tip of the coat, a spontaneous mean curvature cap $C_0 = C_p$ with zero spontaneous deviatoric curvature ($D_0 = 0$) (region 1 in Figure 2a,b),
ii. the rest of the coat with equal values of spontaneous mean and deviatoric curvature $C_0 = D_0 = C_p/2$ (region 2 in Figure 2a,b).
Note that this type of spontaneous curvature distribution arises when BDPs are aligned axially in the hemispherical region (region 1 in Figure 2a) and circumferentially in the cylindrical region (region 2 in Figure 2a). This orientation arises from the minimization of bending energy of the BAR proteins (*36*, *37*). At the pole, the difference between the

two principal curvatures vanishes and therefore has zero deviatoric curvature (Equation (2)). In the cylindrical region, mean and deviatoric curvature are equal; therefore, a circumferential orientation of proteins that allows the spontaneous mean and the deviatoric curvature to be equal minimizes the orientation energy of proteins.

2.2 Free Energy of the membrane

The free energy of the membrane is similar to the elastic energy given by the Helfrich Hamiltonian (*20*) modified to include the deviatoric components (*25*, *26*, *35*)

$$W = \kappa(H - C_0)^2 + \kappa_d(D - D_0)^2, \tag{5}$$

where κ, κ_d are the bending rigidities, H and D are the mean and deviatoric curvatures of the membrane, and C_0, D_0 are the spontaneous isotropic and deviatoric curvatures induced by proteins respectively.

2.3 Governing equations

Local stress balance on the membrane gives us (*38–40*)

$$\boldsymbol{T}^{\alpha}_{;\alpha} + p\boldsymbol{n} = \boldsymbol{0}\,, \tag{6}$$

where p is normal pressure on the membrane and $\boldsymbol{T}$ is the surface stress tensor. Equation (6) results in force balance equations in the tangential and normal direction of the membrane (see Appendix A.2 in the supporting information). The tangential force balance relation reduces to (*26*, *33*, *39*, *40*)

$$\lambda_{,\alpha} = -W_{,\alpha|exp}, \tag{7}$$

where λ is the Lagrange multiplier for area constraints. Physically it represents the tension in the plane of the membrane (*32*, *41–43*). $W_{,\alpha|exp}$ in Equation (7) represents the explicit dependence of the energy on the coordinates (*39*, *40*). The normal force balance relation depicts the equilibrium shape of the membrane and is given by (*26*)

$$\begin{gathered}\frac{1}{2}[W_D(\zeta^\alpha\zeta^\beta - \mu^\alpha\mu^\beta)]_{;\beta\alpha} + \frac{1}{2}W_D(\zeta^\alpha\zeta^\beta - \mu^\alpha\mu^\beta)b_{\alpha\gamma}b^\gamma_\beta + \Delta(\frac{1}{2}W_H) + \\ (W_K)_{;\beta\alpha}(2Ha^{\beta\alpha} - b^{\beta\alpha}) + W_H(2H^2 - K) + 2H(KW_K - W) - 2H\lambda = p.\end{gathered} \tag{8}$$

Here $\boldsymbol{\zeta}$ is the direction of orientation of the BDP's, $\boldsymbol{\mu} = \boldsymbol{n} \times \boldsymbol{\zeta}$, with $\boldsymbol{n}$ as the unit surface normal (*26*).

2.4 Governing equations in axisymmetry

We parametrize Equations (7) and (8) in axisymmetric coordinates for computational tractability. In polar coordinates, the membrane surface can be parameterized by

$$\boldsymbol{r}(r, z, \theta) = \boldsymbol{r}(s, \theta), \tag{9}$$

where s is the arclength, and θ angle in the azimuthal direction. In the limit of axisymmetry, $\frac{\partial(\cdot)}{\partial\theta} = 0$ and the membrane can be parameterized by the arclength s only, as shown in Figure 2.

In axisymmetry, the tangential force balance relation in Equation (7) reads as

$$\lambda' = 2\kappa(H - C_0)C_0' + 2\kappa_d(D - D_0)D_0', \tag{10}$$

where $(\cdot)' = \frac{\partial(\cdot)}{\partial s}$. The normal force balance relation in Equation (8) simplifies to

$$p = \frac{L'}{r} + 2\kappa(H - C_0)\left(2H^2 - K\right) - 2H\left(W + \lambda - 2\kappa_d D(D - D_0)\right). \tag{11}$$

Here we define

$$\frac{L}{r} = [\kappa(H - C_0) - \kappa_d(D - D_0)]' - 2\kappa_d(D - D_0)\frac{\cos\psi}{r}, \tag{12}$$

which is the normal component of traction on the membrane. We note that all of these equations are presented in (*26*) but there is a missing term in L in that work; a complete derivation is presented in Appendix B.1.

2.5 Numerical methods

We solved the system of equations (Equation (S33) to Equation (S35)) numerically to get the equilibrium shape of the membrane for a coat of protein at the center of an axisymmetric area patch. The solution domain is presented in Figure 2a, along with the input protein coat and the boundary conditions (Figure 2a,b). The protein coat includes both the spontaneous mean curvature cap and a combination of mean and deviatoric spontaneous curvature in the rest of the coat region (Figure 2). Note that we introduced a shape variable ψ, which denotes the angle made by the tangent from its radial plane. The membrane is clamped at the domain boundary, where both the displacement and the angle $\psi = 0$. The membrane tension is also prescribed at the boundary. At the pole, ψ is taken to be zero, which indicates the smoothness at the center of the membrane. L is set to zero, indicating that there is no pulling force acting at the center. This distinguishes our work from force-mediated tubulation that was studied in other works (*4*, *5*). To solve the system of equations, we used MATLAB-based bvp4c, a finite difference-based ODE solver with fourth-order accuracy (MATLAB codes are available https://github.com/Rangamani-Lab/arijit_deviatoric_tube_2022). We used a nonuniform grid ranging from 1000 to 10000 points, with the finer grid towards the center. We used a large domain size of 10^6 nm^2 to avoid boundary effects but we show the results focusing on the membrane deformation (region enclosed by the dashed line in Figure 2c).

3 Results

Here we establish the effect of different parameters on the formation of a cylindrical membrane tube and show that membrane tension and bending rigidity govern the energy landscape of tubule formation due to proteins inducing deviatoric curvature. Using numerical simulations, we show that this energy landscape is governed by a snapthrough instability, and different parameters such as area of induced curvature and extent of induced curvature tune the location of the snapthrough transition.

3.1 Membrane tension and bending rigidity regulate the tubule characteristics in the presence of curvature inducing proteins.

We previously showed that membrane tension regulates the formation of spherical vesicles (*33*) and it is well-established that membrane tension governs the force-length relationships of force-mediated tube formation (*4*). How does tension regulate the formation of protein-induced membrane tubules? To answer this question, we first fixed the coat area and the deviatoric curvature and varied membrane tension (Figure 3a-c). We found that, for a fixed coat area of $37,700$ nm^2, low values of deviatoric curvature $D_0 = 0.010$ nm^{-1} were not sufficient to induce the formation of cylindrical structures for the range of membrane tension tested ($\lambda_0 = 0.001, 0.01, 0.1$ pN/nm). The deformations in these cases were dome-shaped without any cylindical portions (multiple z values for a given r). However, when the value of the protein-induced curvature was increased to $D_0 = 0.015$ nm^{-1} (Figure 3b) and to $D_0 = 0.017$ nm^{-1} (Figure 3c), we found that lower values of tension promoted the formation of cylindrical tubules. These results indicate that for a fixed coat area, the combination of induced-curvature and tension regulate the transition from dome-shaped deformations to cylindrical deformations. We then investigated how the area of the coat would affect these transitions (Figure 3d-f) for a fixed amount of induced curvature, $D_0 = 0.015$ nm^{-1}. We found that lower coat area favored dome-shaped deformations even at low tension (Figure 3d) but higher coat area promoted the formation of cylindrical tubes (Figure 3e, f) and the length of the tube increased with decreasing tension.

We next asked if the bending rigidity of the membrane also played a role in the formation of cylindrical tubes. The characteristic length scale of the membrane is $\sqrt{\kappa/2\lambda}$ and therefore, if tension were to be fixed constant but bending rigidity were to change, we would expect to see similar results. We fixed the coat area and protein-induced curvature and varied the bending ridigity of the membrane for a fixed value of membrane tension (Figure 4). For low values of protein-induced curvature, $D_0 = 0.010$ nm^{-1}, the membrane deformation remained dome-shaped for all values of membrane bending rigidity (Figure 4a). Increasing the protein-induced curvature increased the deformation and resulted in cylindrical tubules for higher values of bending rigidity (Figure 4b,c). We observed the same trend for fixed protein-induced curvature and increasing coat area (Figure 4d-f). Smaller coat areas maintained a dome-shaped deformation but larger coat areas resulted in cylindrical tubes as the bending rigidity increased.

It is not surprising that decreasing membrane tension increased tubulation and this is consistent with experimental observations (*44*). However, it may seem counterintituitive that higher membrane modulus promotes tubulation. This result can be understood as follows – in all our simulations, we already prescribe the spontaneous curvature *a priori* and it does not evolve with the shape of the membrane. In other words, the membrane is conforming to a shape that minimizes the energy for a given value of D_0 and the prescribed boundary conditions. For a tensionless membrane,

with free boundaries, the membrane will conform to a cylinder such that it takes on the curvature that is prescribed. Since we have prescribed a boundary condition with a finite tension λ_0, this will promote flattening of the membrane and an increase in bending rigidity will oppose this flattening. Thus, the competition between the bending energy trying to form a cylinder versus the edge tension trying to flatten the membrane results in increased bending rigidity promoting cylindrical tube formation. We revisit the interplay between the membrane bending rigidity and protein-induced curvature in Section 3.5.

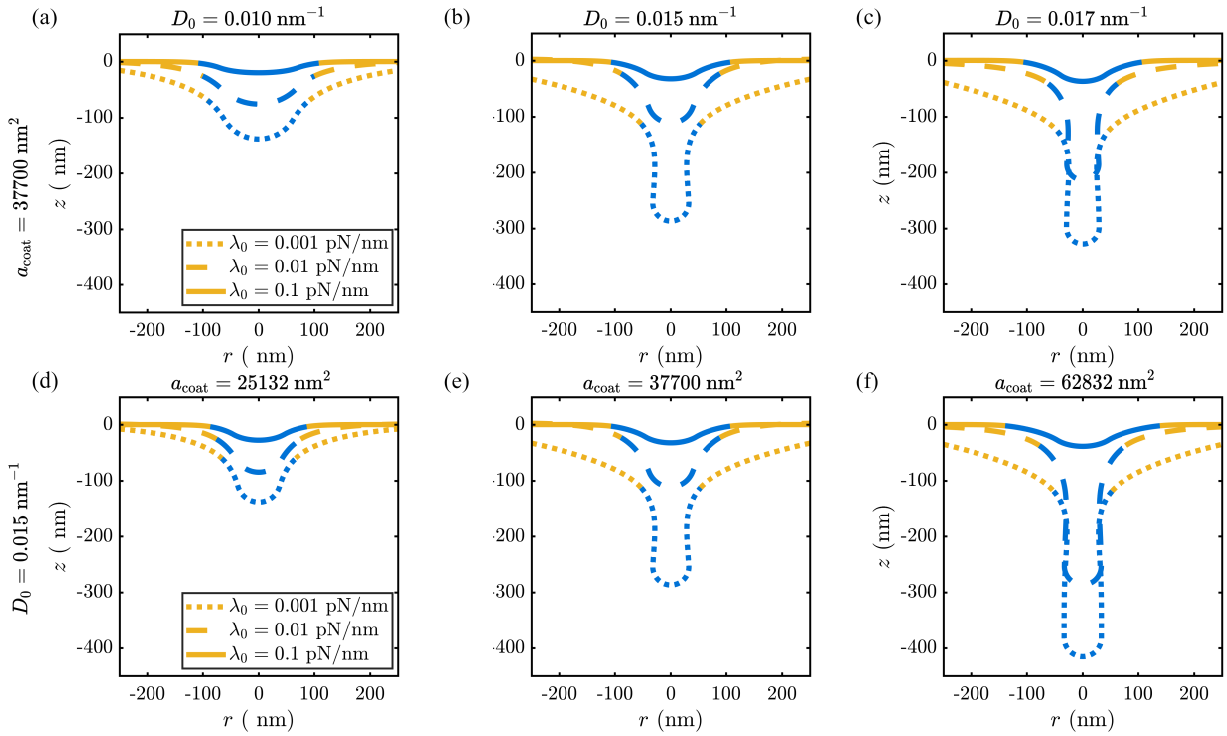

Figure 3: Membrane tension governs tubulation. (a-c) Equilibrium shapes of the membrane for 3 different spontaneous deviatoric curvatures, (a) $D_0 = 0.010$ nm^{-1}, (b) $D_0 = 0.015$ nm^{-1}, and (c) $D_0 = 0.017$ nm^{-1}. For each value of deviatoric curvature, we investigated tubule formation at three different values of tension (0.001, 0.01, 0.1 pN/nm). The area of the protein coat was fixed at 37700 nm^2 and bending rigidity of the membrane was taken to be 42 pN $\cdot$ nm, which is roughly 10 k_BT. (d-f) Equilibrium shape of the membrane for 3 different protein coats areas, (d) $a_{\text{coat}} = 25312$ nm^2, (e) $a_{\text{coat}} = 37700$ nm^2, and (f) $a_{\text{coat}} = 62832$ nm^2 for three different values of tension (0.001, 0.01, 0.1 pN/nm). The spontaneous deviatoric curvature was fixed at 0.015 nm^{-1} and bending rigidity of the membrane 42 pN $\cdot$ nm, which is roughly 10 k_BT.

3.2 Scaling relationships for tube radius and tube length

Given that the formation of a cylindrical tubule depends on multiple parameters such as tension, bending modulus, and the extent of curvature induced by the proteins, we derived scaling relationships to relate these different mechanical properties to the geometry of the cylinder. Motivated by the analysis in (*4*), we considered the free energy of a cylindrical membrane of radius R and length l whose entire area is covered by proteins that induce a curvature of D_0. We ignore the hemispherical cap and the edge conditions. In this case, the free energy of a cylinder is given by

$$E = 4\pi R l \left\{ \kappa \left(\frac{1}{2R} - D_0 \right)^2 \right\} + \lambda_0 2\pi R l. \tag{13}$$

We can obtain radius by minimizing the energy with the radius of the tube R. The variation of energy E with R is given by

$$\begin{aligned} \frac{\partial E}{\partial R} &= 4\pi R l \left\{ 4\kappa \left(\frac{1}{2R} - D_0 \right) \left(-\frac{1}{2R^2} \right) \right\} + \lambda_0 2\pi l \\ &= 4\pi\kappa l \left(\frac{1}{2R} - D_0 \right) \left(\frac{1}{2R} - D_0 - \frac{1}{R} \right) + \lambda_0 2\pi l \\ &= -4\pi\kappa l \left(\frac{1}{4R^2} - D_0^2 \right) + \lambda_0 2\pi l. \end{aligned} \tag{14}$$

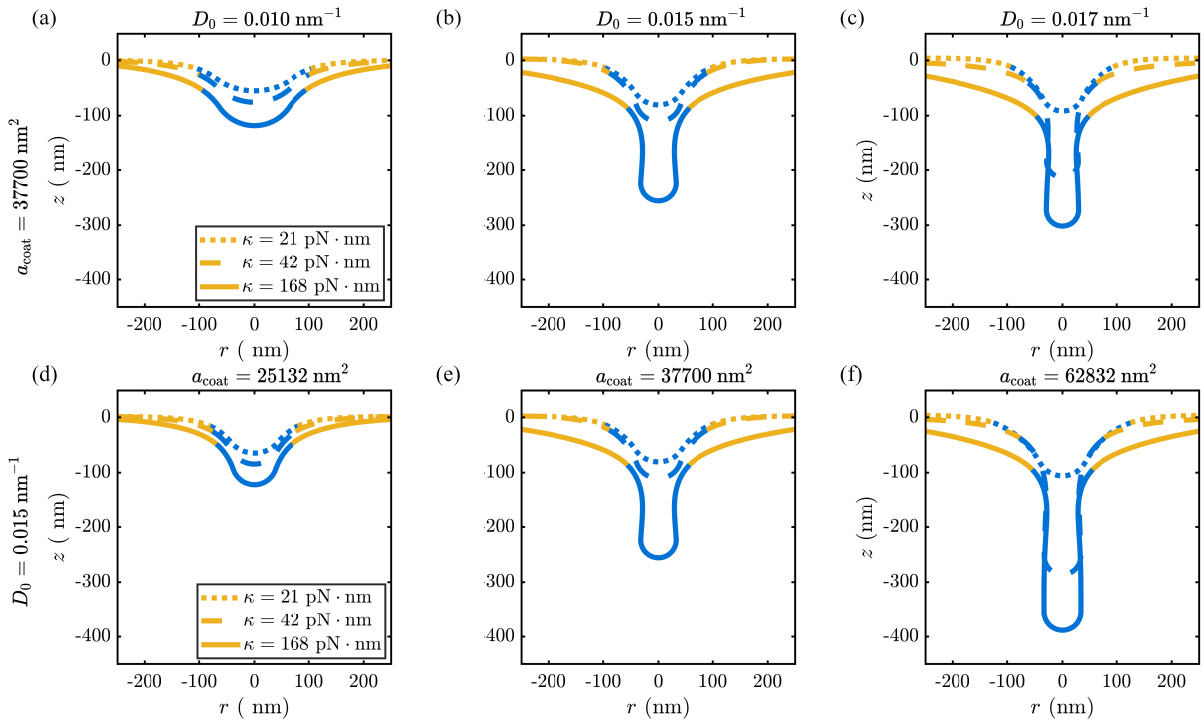

Figure 4: Bending rigidity impacts membrane tubulation. (a-c) Equilibrium shape of the membrane for 3 different spontaneous deviatoric curvatures, (a) $D_0 = 0.010$ nm^{-1}, (b) $D_0 = 0.015$ nm^{-1}, and (c) $D_0 = 0.017$ nm^{-1}. For each value of deviatoric curvature, we investigated tubule formation at three different values of bending ridigity (21, 42, and 168 pN · nm). The area of the protein coat was fixed at 37700 nm^2 and the tension was fixed at 0.01 pN/nm. compared with three different values of bending rigidities (21, 42, 168 pN · nm). (d-f) Equilibrium shape of the membrane for 3 different protein coats areas, (d) $a_{\text{coat}} = 25312$ nm^2, (e) $a_{\text{coat}} = 37700$ nm^2, and (f) $a_{\text{coat}} = 62832$ nm^2 for three different values of bending ridigity (21, 42, and 168 pN · nm). The area of the protein coat was fixed at 37700 nm^2 and the tension was fixed at 0.01 pN/nm.

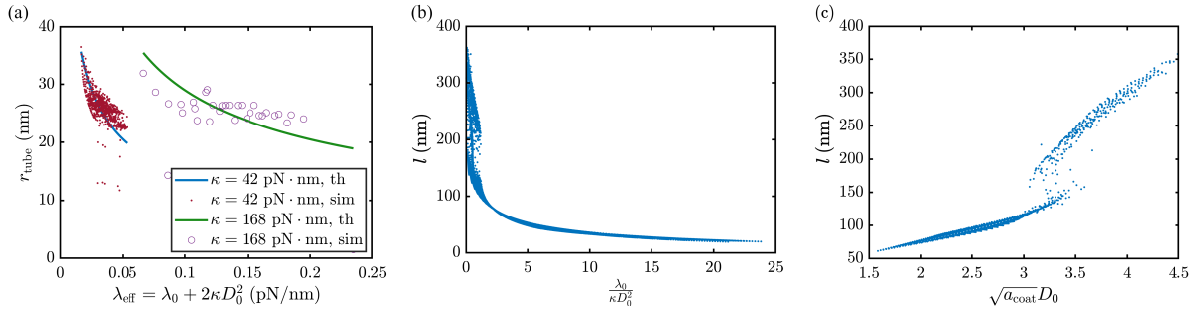

Figure 5: Scaling relationships for tube radius and tube length. (a) Effective tension ($\lambda_{\text{eff}} = \lambda_0 + 2\kappa D_0^2$) governs the radius of the tubular protrusions. A comparison of tube radii from theoretical prediction and numerical simulations for two different values of κ is shown. The solid curves are from the theoretical values in Equation (16) and the dots are from numerical simulations for different values of λ_0 and D_0. The simulations deviate from the theoretical predictions because of edge conditions and the hemispherical cap. (b) Length of the tube scales with $\lambda_0/(\kappa D_0^2)$ and with $\sqrt{a_{\text{coat}}} D_0$ (c). In both these cases, a transition is observed in the nature of the curve around $l = 150 - 200$nm, suggesting a transition in the energy of the tube. For panel (b) protein coat area was fixed at 3.77×10^4 nm^2. For panel (c), bending rigidity was fixed at $\kappa = 42$ pN · nm and tension at λ_0 of 0.01 pN/nm.

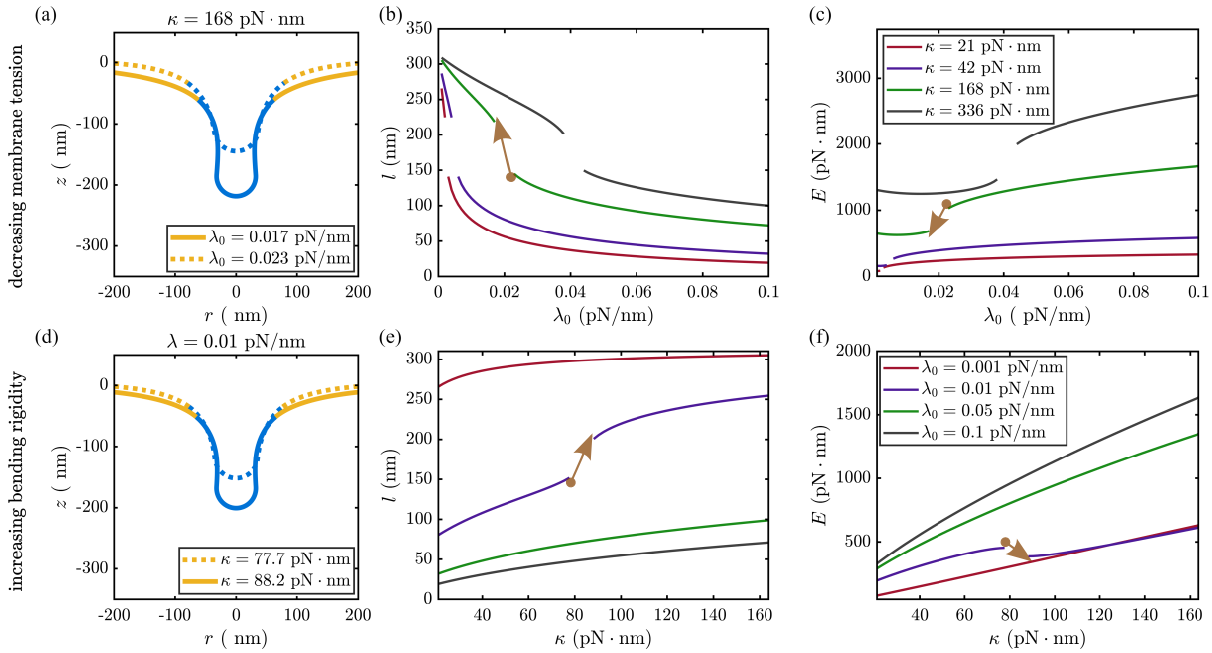

Figure 6: The dome-to-cylinder transition is governed by a snapthrough instability. (a,b,c) Snapthrough instability caused by decreasing membrane tension membrane tension with $a_{\text{coat}} = 3.77 \times 10^4$ nm^2 and $D_0 = 0.015$ nm^2 with the landscape of energy and membrane deformation. (a) The shape of the membrane before (dashed) and after (solid line) after the transition is shown. Both the length of the tubular structure (b) and the bending energy (c) have discontinuities across the snapthrough for different values of bending rigidity κ. (d,e,f) Snapthrough instability caused by increasing bending rigidity κ with $a_{\text{coat}} = 3.77 \times 10^4$ nm^2 and $D_0 = 0.015$ nm^2 with the landscape of energy and membrane deformation. The morphology of the membrane changed from dome to a cylinder shape (d). The length of the tubular structure (e) and the bending energy (f) are shown with bending rigidity for different values of membrane tension. Snapthrough occurs for $\lambda_0 = 0.01$ pN/nm.

Energy minimization results in

$$R = \frac{1}{\sqrt{\frac{2\lambda_0}{\kappa} + 4D_0^2}} \tag{15}$$

$$= \sqrt{\frac{\kappa}{2\lambda_{eff}}}. \tag{16}$$

where $\lambda_{eff} = \lambda_0 + 2D_0^2\kappa$ is an effective tension. This relationship is reminiscent of the radius of a tube extruded using a pulling force, $R = \sqrt{\kappa/2\lambda}$ (*4*), with an effective tension λ_{eff} that accounts for the tension contributions from the protein coat (*31*, *41–43*). We compared our theoretical prediction against simulations for two different values of κ (Figure 5a). We found that the values from the simulations were very close to the theoretically predicted curves; the deviations are a result of the boundary conditions and the hemispherical cap in the simulation geometry.

We note that there is no equivalent relationship for force on the tip of the tube because our energy does not contain a force term. Therefore, we cannot obtain a scaling relationship for the length of the tube with the forces applied at the tip of the tube. Instead, we sought dimensionless numbers from the governing equations that could describe the length of the tube in a reduced parameter space. We constructed these dimensionless numbers using the Buckingham-Pi theorem as a function of characteristic scales. We found that the length of the tube for different conditions collapses to a line as a function of $\frac{\lambda_0}{\kappa D_0^2}$ (Figure 5b). These simulations were performed for different values of λ_0, κ, and D_0 keeping coat area, a_{coat}, constant. We further observe a transition in the length around 200 nm indicating a change in nature of the system. We also observed that the length of the tube collapses onto a line with another dimensionless number $\sqrt{a_{\text{coat}}}D_0$ (Figure 5c). This is because the tube length depends not only on the membrane parameters but also on the area of the coated region. Again, we observe a transition in the nature of the length of the tube around $150 - 200$ nm, depicted by a decreasing density of points.

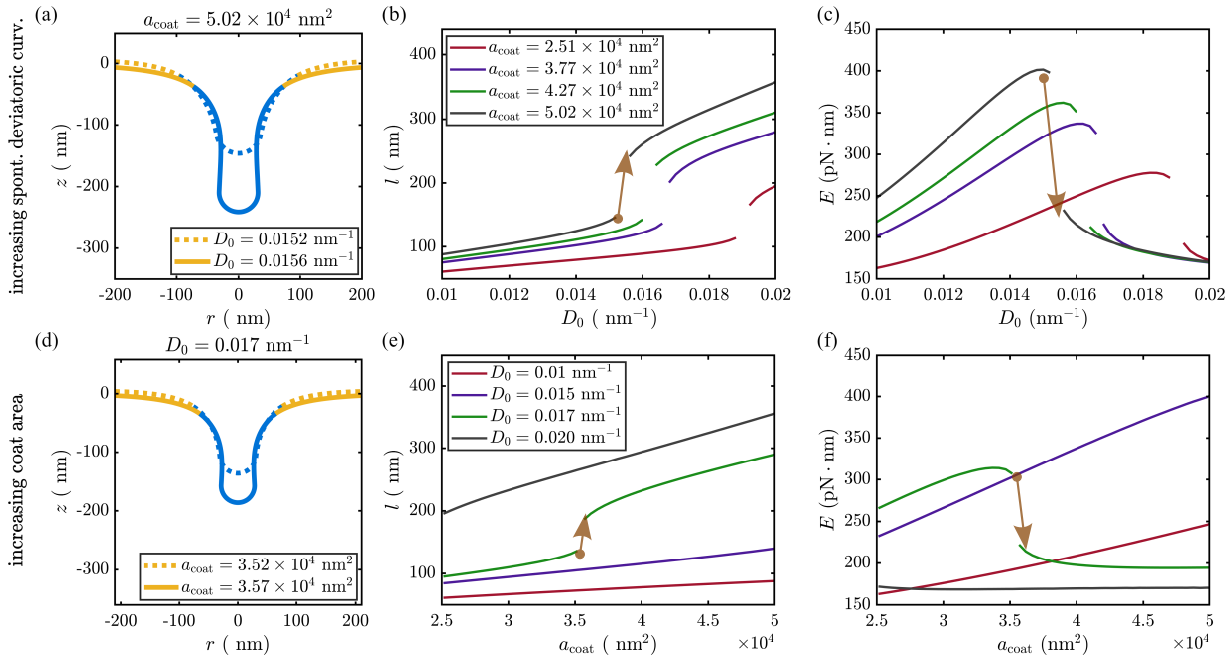

Figure 7: The role of spontaneous deviatoric curvature and the coat area on snapthrough instability. (a,b,c) Snapthrough instability caused by increasing spontaneous deviatoric curvature with $\kappa = \kappa_d = 42$ pN · nm and $\lambda_0 = 0.01$ pN/nm^2 with the landscape of energy and membrane deformation. Both the length of the tubular structure (b) and the bending energy (c) experienced discontinuities across the snapthrough, and are shown for 4 different values of bending rigidity κ. The morphology of the membrane changed from dome to cylinder shape (a). (d,e,f) Snapthrough instability caused by increasing coat area of protein with $\kappa = \kappa_d = 42$ pN · nm and $\lambda_0 = 0.01$ pN/nm^2 with the landscape of energy and membrane deformation. The length of the tubular structure (e) and the bending energy (f) are shown with bending rigidity for different values of membrane tension. For $\lambda_0 = 0.01$ pN/nm, a discontinuity is observed where the morphology of the membrane changed from dome to cylinder shape (d).

3.3 Formation of cylindrical tubes is governed by a snap-through instability

In our simulations, we observed that the transition from a dome-shaped cap to a cylindrical tube appeared as an abrupt transition (Figures 3 and 4) accompanying the elongation of the tube (Figure 5). We conducted further simulations around regions of these abrupt transitions and investigated the energy landscape (Figure 6). As before, we fixed the bending rigidity and decreased the membrane tension (Figure 6a-c). We found that the dome-to-cylinder transition took place between $\lambda_0 = 0.023$ pN/nm and $\lambda_0 = 0.017$ pN/nm. This transition is accompanied by the formation of a cylinder, where multiple z values have the same r (Figure 6a). The abrupt nature of this transition is evident by studying the length as a function of tension for different bending rigidity values (Figure 6b). For all values of bending rigidities investigated, we found that decreasing tension resulted in the elongation of the cylinder and the discontinuity indicated the presence of a snapthrough instability. This discontinuity in length is accompanied by a discontinuity in the energy landscape, such that decreasing tension results in a jump from a high energy state to a low energy state (Figure 6c). A similar transition can also be seen when the bending rigidity is varied (Figure 6d-f). The transition from a dome-shaped deformation to a cylinder occurs between $\kappa = 77.7$ pN · nm and $\kappa = 88.2$ pN · nm, while all other parameters are held constant (Figure 6d). However, the snapthrough transition occurs only for specific values of membrane tension (Figure 6e). For example, low tension values result in long tubes and high tension values result in dome-shaped membranes for a wide range of bending rigidities. At intermediate values of tension, we observe a snapthrough instability as a discontinuity in the increasing length of the membrane for increasing rigidity and a corresponding drop in energy (Figure 6f).

The snapthrough behavior of elastic membranes can be demonstrated by saddle node bifurcations (*45*). However, the nonlinear nature of the present problem precludes stability analysis since closed-form solutions of the governing equation are not possible. We sought to use a numerical approach to demonstrate the snapthrough. We expect a pair of stable equilibrium solutions in the neighborhood of the transition to demonstrate the existence of saddle node bifurcations. We conducted simulations by varying tension in the increasing and decreasing direction and using the solution of the previous parameter value as an initial guess for the current parameter value. As we traverse the tension axis, we find that there are two different solutions for the minimum energy shape of the membrane and there is a lag in

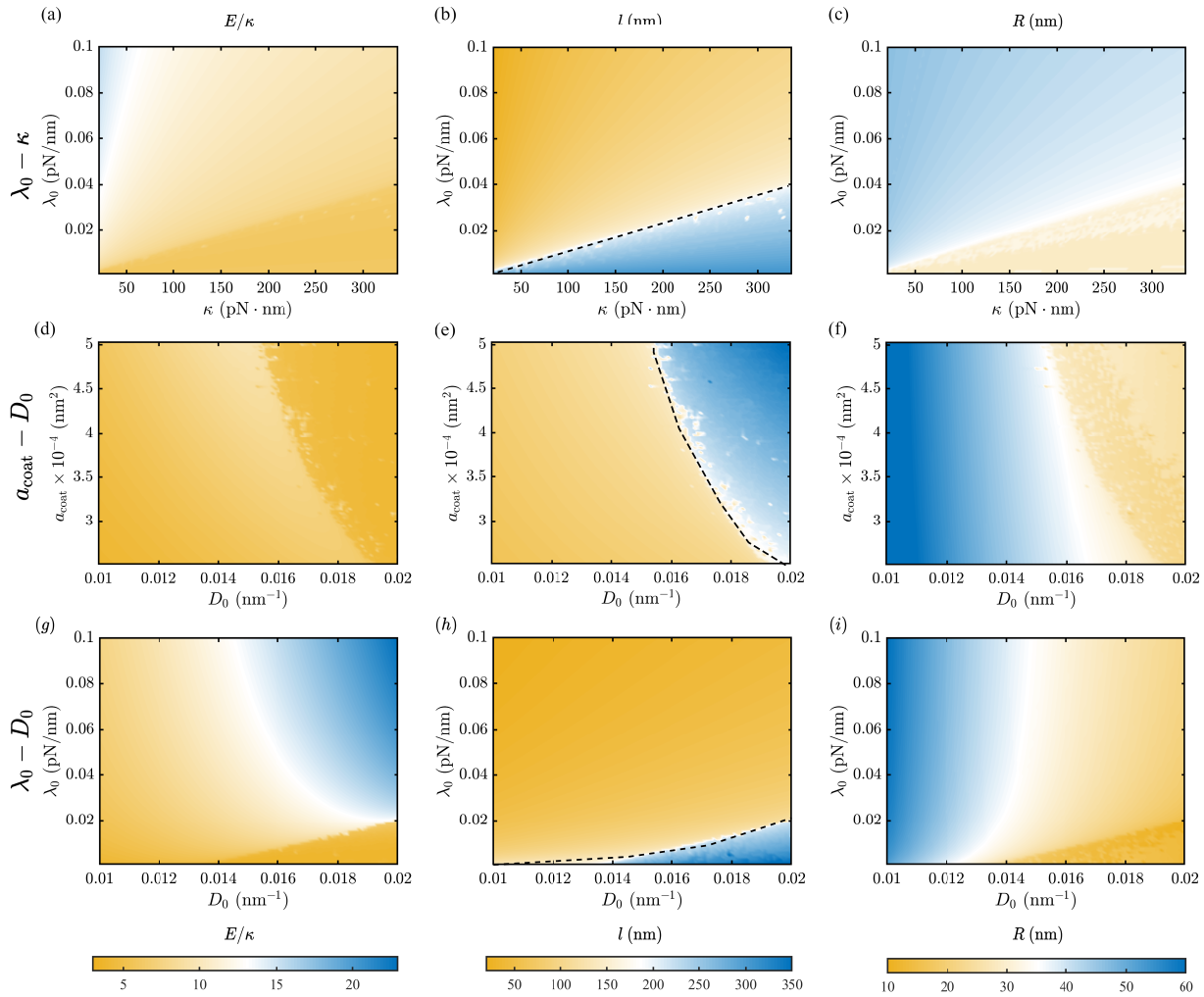

Figure 8: The dome-to-cylinder transition is depicted by the energy landscape in the parameter spaces membrane tension (λ_0), bending rigidity (κ), coat area of protein (a_{coat}), and the spontaneous curvatures (D_0). We present the phase-space of bending energy, length and radius of the tube in the parameter space of $\lambda_0 - \kappa$ (a-c) for $a_{\text{coat}} = 37700$ nm^2 and $D_0 = 0.015$ nm^{-1}, $a_{\text{coat}} - D_0$ (d-f) for $\kappa = 42$ pn · nm and $\lambda_0 = 0.01$ pN/nm, and $\lambda_0 - D_0$ (g-i) for $a_{\text{coat}} = 37700$ nm^2, $\kappa = 42$ pN · nm. The first column (a,d,f) shows the ratio of bending energy to the bending rigidity. Note that bending energy E varies directly with κ, therefore for $k = 336$ pN · nm E becomes as high as 3000 pN · nm in the parameter space of $\lambda_0 - \kappa$, whereas, for other two parameter space maximum value of E is around 1000 pN · nm. To represent the variation in the same color scale we normalized the bending energy with κ, and noticed sharp energy change across the dome to cylinder transition, which is much more evident in the phase diagram of the length l as shown with a dashed line (b,e,h). However, the change in radius across this length transition is not as dramatic as the tube length; nonetheless, we notice a transition, as shown by the color contrast from dark yellow to light yellow (c,f,i).

the tube length and bending energy when we change λ_0 in forward and backward directions (Figure S2). Thus using numerical solutions, we show that the transition from dome-to-cylinder is indeed a snapthrough instability.

We next investigated the effect of varying the protein-induced curvature D_0 and coat area a_{coat} on the snapthrough transition (Figure 7). For a fixed coat area, we found that the snapthrough transition occurs for increasing coat curvature (Figure 7a). We see a sharp increase in tube length (Figure 7b) and a corresponding decrease in bending energy drops at the transition (Figure 7c). Similar transitions can be seen for increasing the coat area for a fixed value of protein-induced curvature (Figure 7d). In this case, we see that length of the tube has a discontinuity with increasing coat area for a specific value $D_0 = 0.017\,\text{nm}^{-1}$ (Figure 7e) and this corresponds to a sharp decrease in the bending energy (Figure 7f). For the other values of D_0 tested, we did not observe any transition – a cylinder remains as a cylinder and a dome remains a dome in these cases. The corresponding energies are also monotonic.

3.4 Phase diagrams show transition boundaries for different tube parameters

Our results thus far indicate that the transition from a dome-shaped deformation to a cylindrical tube is governed by a snapthrough instability that depends on multiple parameters such as protein-induced curvature, bending rigidity, edge tension, and coat area. In order to understand how these parameters affect tube length, tube radius, and bending energy, we systematically varied them in physically relevant ranges (Table 2). For each parameter combination, we plot the tube length, tube radius, and the bending energy (Figure 8). In the tension-bending rigidity space, the energy landscape shows a curved surface where high bending rigidity has high bending energy but increasing tension lowers the bending energy for all values of bending rigidity (Figure 8a). The length of the tube had a smooth and linear transition from short tubes to long tubes (Figure 8b). A similar transition is seen for the tube radius; thicker tubes are formed for higher tension and thinner tubes for higher bending rigidity (Figure 8c).

In the coat area and protein-induced curvature space, the bending energy landscape is non-monotonic and shows a highly curved manifold where the bending energy increases as coat area increases and remains low as coat curvature increases (Figure 8d). For this combination of parameters, the transition from short to long tubes in nonlinear but consistent with our understanding that higher induced curvature and larger area are compatible with longer tubes (Figure 8e). The tube radius shows little-to-no dependence on coat area but depends on the protein-induced curvature with smaller curvatures resulting in larger tube radii (Figure 8f). Finally, we investigate the tension-induced-curvature landscape and find that the tube length remains small for most values of tension for all values of induced-curvature. The bending energy remains low for most values of tension and induced curvature, increasing for high values of induced curvature (Figure 8i). Only when the tension value is low do we obtain long tubes (Figure 8h). The tube radius has a weak dependence on tension for low and high values of induced curvature (Figure 8i). At intermediate values, there is a nonlinear dependence on both tension and induced curvature, consistent with the dependence of tube radius on effective tension (see Equation (16) and Figure 5a).

3.5 Effective spontaneous curvature and the role of bending rigidity

Thus far, we have assumed that the proteins are rigid and non-deformable. Therefore, in all our simulations, we prescribed spontaneous curvature without accounting for the deformability of the protein and the resulting interaction with the membrane. As a result, we find that a membrane with higher bending rigidity accommodates a tubular shape when compared to a membrane of lower bending rigidity (Figure 6e and Figure 8b, which is counterintuitive. What we would expect and what we know from experimental observations is that a membrane with higher bending rigidity will offer more resistance to deformation. Therefore, it should be easier to form tubes on softer membranes. To address this discrepancy, we revisited our previous assumption that the proteins are rigid and non-deformable and accounted for protein deformability. For a deformable BAR-domain protein, the effective spontaneous curvature, C_eff, that it can induce depends on its intrinsic spontaneous curvature C_p, the bending modulus of the protein κ_p and the membrane bending modulus κ and can be understood from a simplified calculation for a 1D protein as shown in Figure 9a. The free energy of bending of the membrane-protein composite, $\mathcal{F}$, is the sum of the bending energy of the membrane for deformation from a flat shape to a curved shape and the energy of bending for protein associated with the change of curvature of $(C_p - C_{eff})$ (see Figure 9a),

$$\mathcal{F} = \kappa C_{eff}^2 + \kappa_p \left(C_{eff} - C_p\right)^2 . \tag{17}$$

The resulting effective curvature C_{eff} can be obtained by minimizing free energy of the membrane and is given by

$$\frac{\delta \mathcal{F}}{\delta C_{eff}} = 0 \Rightarrow C_{eff} = \frac{\kappa_p C_p}{\kappa + \kappa_p}. \tag{18}$$

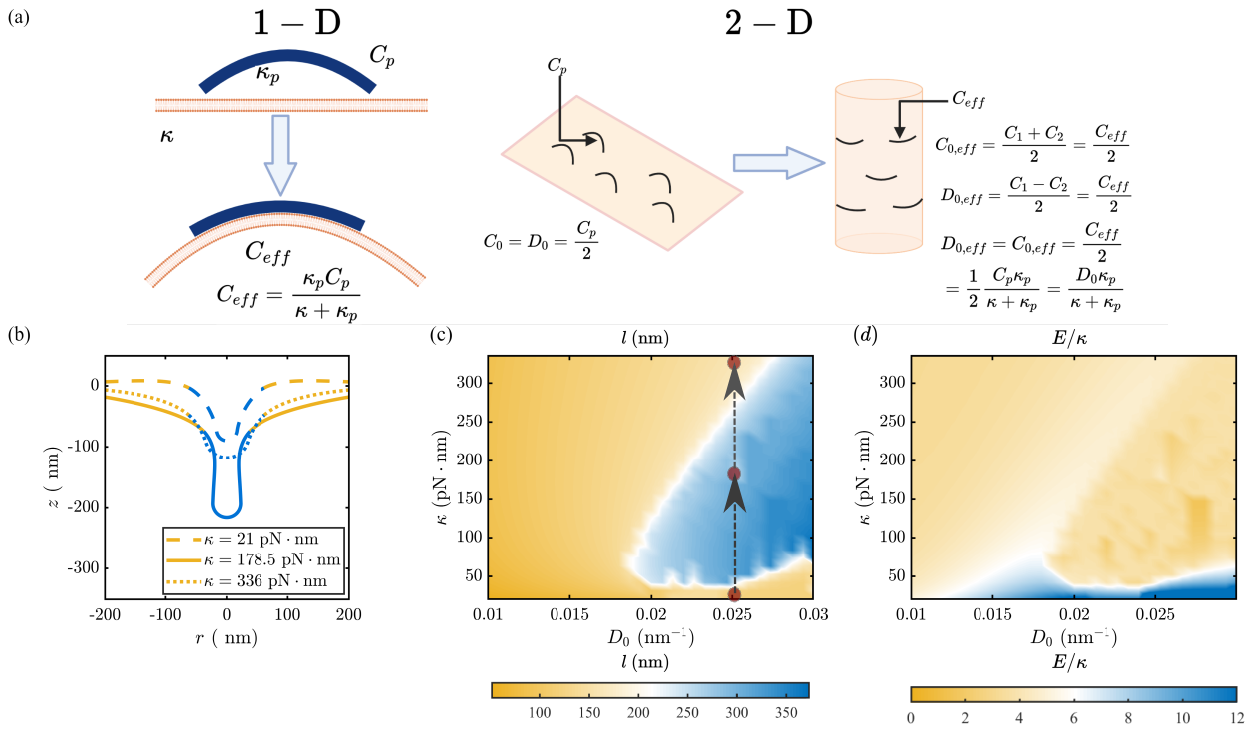

Figure 9: Effective spontaneous curvature generated by BAR-domain proteins on the membrane and its impact on tube formation. (a) Schematic of effective spontaneous curvature of flexible protein with bending rigidity κ_p and intrinsic curvature C_p to a flat membrane with bending rigidity κ in 1-D and 2-D. (b) Shapes of the membrane based on the calculated effective spontaneous curvature (Equation (17)) with intrinsic spontaneous curvatures $C_0 = D_0 = 0.025$ nm^{-1}, coat area of 37700 nm^2, membrane tension 0.01 pN/nm, and for three different values of bending rigidity. (c) Dome-to-cylinder transition with tube length in the plane of $\kappa - D_0$ for coat area of 37700 nm^2, membrane tension 0.01 pN/nm. (d) The landscape of ratio between bending energy and bending rigidity of membrane in the plane of bending $\kappa - D_0$ for coat area of 37700 nm^2, membrane tension 0.01 pN/nm.

For two different values of κ and for the same values of C_p and κ_p, the ratio of effective spontaneous curvatures becomes $\frac{C_{eff,1}}{C_{eff,2}} = \frac{\kappa_2+\kappa_p}{\kappa_1+\kappa_p}$. Thus, as the bending stiffness increases, the effective spontaneous curvature decreases. On the other hand, when we consider a fixed spontaneous curvature for membranes with different bending rigidities, the ratio of intrinsic curvature becomes $\frac{C_{p,1}}{C_{p,2}} = \frac{\kappa_1+\kappa_p}{\kappa_2+\kappa_p}$. Therefore, when we previously modeled a stiffer membrane, we actually considered a higher curvature induced by the protein. This effect combined with the reduction in the dimensionless tension $\frac{\lambda_0 L^2}{\kappa}$ for higher bending rigidity results in promotes tube formation at higher bending rigidity.

To fully demonstrate the effect of Equation (17), we simulated the minimum energy shapes of the membrane as before. To convert the simple 1-D model in Figure 9a to relevant parameters that can be input in the axisymmetric simulations, we recall that $C_0 = D_0 = C_p/2$ (Equation (4)). The governing equations (Equation (S33) to Equation (S35)) take effective curvatures C_{eff} and D_{eff} as their inputs. These values are calculated for a given value of C_p or equivalently D_0 (see Figure 9a). We varied the intrinsic spontaneous curvatures of proteins C_p, such that D_0 varies from 0.01-0.03 nm^{-1} and bending rigidity of membrane from 21-336 pN · nm (*29*, *30*) We fixed κ_p at 336 pN · nm (*18*). In Figure 9b, we show the shape of the membrane for a coat area of 37700 nm^2 and tension of 0.01 pN/nm for a total membrane area of 377000 nm^2. We found that the tube length increases with increasing bending rigidity and then decreases, indicating a non-monotonic dependence of tube length on membrane bending rigidity. We further investigated this dependence in the phase space of $D_0 - \kappa$ in Figure 9c. In all these simulations, coat area was 37700 nm^2 and tension was 0.01 pN/nm. We observed that for D_0 values below 0.018 nm^{-1}, membranes do not form tubes for any values of bending rigidity. However, for higher spontaneous curvature values, intermediate bending rigidities were favorable for tube formation. For high values of D_0, high bending modulus is not favorable for tube formation and the membrane remains dome shaped. Thus, we predict that for softer membranes (lower κ), tension dominates and resists the membrane to form a tube. For higher bending rigidities, the effective spontaneous curvature reduces significantly, preventing tube formation. However, at intermediate bending rigidity, the effective spontaneous curvature is high enough to deform the membrane and the membrane has enough stiffness to resist the tension effects. As a result, membranes deform into tubes in that region. In Figure 9d, we plot the bending energy in the parameter space of $D_0 - \kappa$ and see how the interplay between $D_0 - \kappa$ space favorable for tube formation corresponding to lower bending energy.

Thus, the formation of a cylindrical tubule due to protein-induced curvature depends on membrane properties and is governed by a snapthrough transition. Furthermore, we predict that the coupling between membrane bending and protein bending can alter this transition.

4 Discussion

In this study, we have presented a theoretical formulation of tube formation due to protein-induced anisotropic curvature and used it to simulate cylindrical tubules without any approximations to boundary conditions. In our continuum approach, we accounted for the effect of orientation that minimizes the bending energy of proteins and is denoted by specified values of spontaneous curvature. Using this model, we identified that the energy landscape of protein-induced tubulation is governed by a snapthrough instability and this instability depends on the membrane tension and bending modulus. This snapthrough is associated with a transition from a dome-to-tube transition in the length of the tubule. Furthermore, we observed a downhill of energy across this transition, suggesting how the bending energy landscape favors the transition of the tube shape.

The idea that deviatoric curvature favors tubular protrusion has been proposed in a series of papers (*26*, *27*, *36*), where a cylindrical membrane is coated with proteins that induce deviatoric curvature. However, formation of tube from a flat membrane due to anisotropic curvature alone (in the absence of any localized force at the pole), has been investigated in only a few studies. Of note is the study by Perutkova *et al.* (*36*), which shows that tubular shapes in the presence of deviatoric curvature are energetically favorable. In studies focused on modeling yeast endocytosis, where the endocytic invagination forms a tube, localized forces were used to model the tubulation and such forces were ascribed to actin (*46–48*). Here we show that anisotropic curvatures such as those induced by BAR-domain proteins are sufficient to form a cylindrical tube.

While surveying the parameter space for tubulation, we observed that the elongation of a tube was governed by a snapthrough instability. We previously reported a snapthrough instability for the formation of a spherical bud (*33*) and find that tubulation is also governed by a similar tension-dependent transition. Additionally, the equivalent effective tension helps us understand the relationship between tube radius and contributions from the different terms. These relationships have implications in biophysical processes where changes of lipid composition and lipid saturation leads to changes in the effective tension (*49*).

Based on our theory and simulations, we make the following experimentally relevant predictions:

- For a given protein-induced anisotropic curvature, low tension is conducive to tube formation. While high tension inhibits tube formation, there are intermediate values of tension for which the transition from a dome-shape deformation to a cylindrical tube is governed by a snapthrough transition. Experimentally, in GUVs for example, this means that the value of tension in the membrane can determine the geometry of the tube even when all other variables are held constant. Thus, our model predicts that the physical interactions between the membrane-bound proteins and the membrane properties itself is important in determining the state of the tube (*8*).
- In cells, this prediction could imply that the heterogeneous tension distribution (*50*) will likely render some regions of the plasma membrane more favorable to tubulation than others.
- The tube radius can be determined by an effective tension, which is combination of bare membrane tension and the spontaneous tension induced by the proteins (*31*). This effective tension, given in Equation (16), can be used to relate experimentally controlled input variables to the tube radius.
- In addition to the tension and bending modulus, the coat area and coat curvature also regulate the snapthrough transition. Experimental inputs related to these variables such as the curvature of proteins and their surface coverage are key to regulate the tube curvature. Since BAR-domain proteins have a variety of radii of curvature (*8*), our model predicts that tuning a few physical parameters can give rise to range of tube geometries. Additionally, our model provides a way of quantifying the effect of such physical parameters.

The predictions from our model have implications for understanding the formation and maintenance of tubular structures generated by proteins in cells such as formation of t-tubule in myocytes (*51*), cristae formation in mitochondria (*52*, *53*), and trafficking from intracellular organelles to the plasma membrane (*54*). The maintenance of t-tubules in muscle cells depends on the distribution of BAR-domain containing proteins called BIN1 among others (*51*, *55*). In heart failure, there is a marked reduction of BIN1 and the t-tubule network is significantly modified leading to loss of excitation-contraction coupling (*56*). Similarly, the maintenance of the tubular invagination in yeast during endocytosis depends on the F-BAR and N-BAR proteins and the absences of these proteins disrupts the progression of endocytosis (*57*).

We note that our present work has a number of simplifications particularly with respect to the protein coat. The binding and unbinding of these anisotropic curvature inducing proteins is curvature dependent (*8*, *19*, *58*). The accumulation of these protein dimers and the interaction between their curvature sensing and curvature generation abilities also depends on their adsorption, diffusion, and aggregation in the plane of the membrane (*59*). Such processes have been studied using molecular dynamics simulations (*17*, *18*) and a continuum description of these process that couples the underlying thermodynamics (*60*, *61*) coupled with membrane deformation would be necessary to avoid the model simplifications. We also anticipate that the interactions between protein-mediated tubulation and force-mediated tubulation would be necessary to capture cellular processes where both membrane-bound proteins and actin-mediated forces are involved (*62*–*64*). Simulations using general coordinates reveal that the early modes of deformation are axisymmetric (*65*). However, relaxation of the assumption of axisymmetry in tubulation would be necessary to investigate how forces and proteins may interact (*65*–*67*). In summary, we expect that the findings from our work will motivate the development of these future efforts and gain a deeper understanding of how membrane tubes form under different biophysical conditions.

Acknowledgments

The authors would like to thank Profs. David Saintillan and Itay Budin for their critical feedback. They would also like to thank Dr. Miriam Bell, Dr. Aravind Chandrasekaran, Dr. Sage Malingen, and Mr. Cuncheng Zhu for their input and discussions. This work was supported by NIH R01GM132106 to P.R.

Supporting Information

A Model Development

A.1 Surface representation

In a polar coordinate the membrane can be parameterized by the arclength s and the rotation angle θ as

$$\boldsymbol{r}(r, z, \theta) = \boldsymbol{r}(s, \theta). \tag{S1}$$

The surface tangents are given by $\boldsymbol{e}_s = \boldsymbol{r}_{,s}$ and $\boldsymbol{r}_{,\theta}$. The surface metric $a_{ij} = \boldsymbol{e}_i \cdot \boldsymbol{e}_j$ becomes

$$a_{ij} = \begin{bmatrix} 1 & 0 \\ 0 & r^2 \end{bmatrix}. \tag{S2}$$

The curvature tensor $b_{ij} = e_{i,j} \cdot \boldsymbol{n}$ simplifies to

$$b_{ij} = \begin{bmatrix} \psi_s & 0 \\ 0 & r \sin \psi \end{bmatrix}. \tag{S3}$$

The mean curvatures is given by

$$H = \frac{1}{2} a^{\alpha\beta} b_{\alpha\beta},$$

where, $a^{\alpha\beta}$ is the inverse of the metric tension. The principal curvature can be extracted from the curvature tensor as

$$c_\zeta = b_{\alpha\beta} \zeta^\alpha \zeta^\beta,$$

and

$$c_\mu = b_{\alpha\beta} \mu^\alpha \mu^\beta.$$

where, $\boldsymbol{\zeta}$ and $\boldsymbol{\mu}$ are surface tangents in two principal directions, The deviatoric curvature becomes

$$D = \frac{1}{2}(c_\zeta - c_\mu).$$

A.2 Protein Orientation

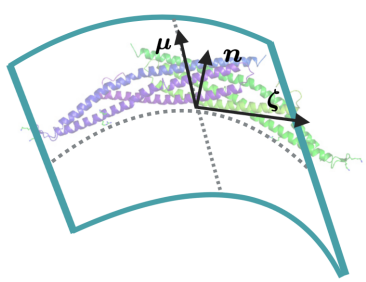

Figure S1: Orientation vectors of BAR-domain proteins

The orientation of a protein on the surface can be represented by orientation unit vector $\boldsymbol{\zeta}$ (Figure S1) which essentially indicates tangent to the curve on which protein orients (*26*). Thus we can constitute another unit vector $\boldsymbol{\mu}$, such that: $\boldsymbol{\mu} = \boldsymbol{n} \times \boldsymbol{\zeta}$.

A.3 Balance relations

The force balance equation is dictated by

$$\boldsymbol{T}^{\alpha}_{;\alpha} + p\boldsymbol{n} = \boldsymbol{0}\,, \tag{S4}$$

where p is normal pressure on the membrane and $\boldsymbol{T}$ is traction on the membrane and given by,

$$\boldsymbol{T}^{\alpha} = N^{\beta\alpha}\boldsymbol{a}_{\beta} + S^{\alpha}\boldsymbol{n}. \tag{S5}$$

Here, $\boldsymbol{N}$ is the in-plane component of the stress and is given by

$$N^{\beta\alpha} = \zeta^{\beta\alpha} + b^{\beta}_{\mu}M^{\mu\alpha} \qquad \text{and} \qquad S^{\alpha} = -M^{\alpha\beta}_{;\beta}, \tag{S6}$$

where $\sigma^{\beta\alpha}$ and $M^{\beta\alpha}$ are obtained from the following constitutive relations (*38*)

$$\sigma^{\beta\alpha} = \rho\left(\frac{\partial F}{\partial a_{\alpha\beta}} + \frac{\partial F}{\partial a_{\beta\alpha}}\right) \quad \text{and} \quad \boldsymbol{M}^{\beta\alpha} = \frac{\rho}{2}\left(\frac{\partial F}{\partial b_{\alpha\beta}} + \frac{\partial F}{\partial b_{\beta\alpha}}\right), \tag{S7}$$

with $F = W/\rho$ as the energy mass density of the membrane. Combining these we get the balance equations in tangent and normal direction

$$N^{\beta\alpha}_{;\alpha} - S^{\alpha}b^{\beta}_{\alpha} = 0, \quad S^{\alpha}_{;\alpha} + N^{\beta\alpha}b_{\beta\alpha} + p = 0 \tag{S8}$$

The normal force balance relation in Equation S8$_{ii}$ becomes (*26*)

$$\begin{aligned}&\underbrace{\frac{1}{2}[W_D(\zeta^{\alpha}\zeta^{\beta} - \mu^{\alpha}\mu^{\beta})]_{;\beta\alpha}}_{\mathrm{I}} + \underbrace{\frac{1}{2}W_D(\zeta^{\alpha}\zeta^{\beta} - \mu^{\alpha}\mu^{\beta})b_{\alpha\gamma}b^{\gamma}_{\beta}}_{\mathrm{II}} + \\ &\Delta\left(\frac{1}{2}W_H\right) + (W_K)_{;\beta\alpha}\left(2Ha^{\beta\alpha} - b^{\beta\alpha}\right) + W_H(2H^2 - K) + 2H(KW_K - W) - 2H\lambda = p,\end{aligned} \tag{S9}$$

where the marked terms are simplified in the next section for an axisymmetric geometry. To construct a force boundary condition we use the expression of the normal traction force as given by (*68*)

$$\begin{aligned}F_n = &(\tau W_K)' - \frac{1}{2}\left(W_H\right)_{,\nu} - \left(W_K\right)_{,\beta}\tilde{b}^{\alpha\beta}v_{\alpha} \\ &+ \frac{1}{2}\left(W_D\right)_{,\nu} - \left(W_D\lambda^{\alpha}\lambda^{\beta}\right)_{;\beta}v_{\alpha} - \left(W_D\lambda^{\alpha}\lambda^{\beta}v_{\beta}\tau_{\alpha}\right)',\end{aligned} \tag{S10}$$

where $\boldsymbol{\tau}$ is the unit tangent to the curve at boundary, $\boldsymbol{\nu}$ is the outward normal to the same curve at the boundary, and can be constructed from local surface normal $\boldsymbol{n}$ as $\boldsymbol{\nu} = \boldsymbol{\tau} \times \boldsymbol{n}$.

B Simplification in axisymmetry

B.1 Governing equations

We have orthogonal surface tangent vectors as given by

$$\boldsymbol{a}_1 = \boldsymbol{e}_s, \quad \boldsymbol{a}_2 = r\boldsymbol{e}_{\theta}. \tag{S11}$$

We get the expression of orientation unit vector in terms of orthogonal basis vectors as given below

$$\boldsymbol{\zeta} = -\boldsymbol{e}_{\theta} = -\frac{1}{r}\boldsymbol{a}_2, \quad \boldsymbol{\mu} = \boldsymbol{a}_1. \tag{S12}$$

We first find the expressions of the direct products of orientation vectors used in Equation (S9) below

$$\zeta^{\alpha}\zeta^{\beta} = \begin{pmatrix} 0 & 0 \\ 0 & 1/r^2 \end{pmatrix}, \tag{S13}$$

and

$$\mu^{\alpha}\mu^{\beta} = \begin{pmatrix} 1 & 0 \\ 0 & 0 \end{pmatrix}. \tag{S14}$$

In the limit of axisymmetry, the components of Christoffel symbols denoted by

$$\Gamma^a_{bc} = \frac{1}{2} a^{ad} \left[\partial_a a_{bd} + \partial_b a_{dc} - \partial_d a_{bc} \right].$$

The components of the Christoffel are given below with 1 and 2 denoting the arclength (s) and azimuthal direction, respectively

$$\begin{aligned} &\Gamma^1_{11} = 0, \quad \Gamma^2_{22} = 0, \quad \Gamma^1_{22} = -r \cos\psi, \\ &\Gamma^2_{12} = \Gamma^2_{21} = \tfrac{\cos\psi}{r}, \quad \Gamma^1_{21} = 0, \text{and} \quad \Gamma^2_{11} = 0. \end{aligned} \tag{S15}$$

We first simplify the term I in Equation (S9) below

$$\begin{aligned} \mathsf{I} &= \frac{1}{2} \left[W_D \left(\zeta^\alpha \zeta^\beta - \mu^\alpha \mu^\beta \right) \right]_{;\beta\alpha} \\ &= (W_D \zeta^\alpha \zeta^\beta)_{;\beta\alpha} - \frac{1}{2} \left[W_D \left(\zeta^\alpha \zeta^\beta + \mu^\alpha \mu^\beta \right) \right]_{;\beta\alpha} \\ &= (W_D \zeta^\alpha \zeta^\beta)_{;\beta\alpha} - \frac{1}{2} (W_D a^{\alpha\beta})_{;\beta\alpha}. \end{aligned} \tag{S16}$$

Note that we recover the surface metric from the addition of the direct products of the orientation vectors as given below

$$\left(\zeta^\alpha \zeta^\beta + \mu^\alpha \mu^\beta \right) = \begin{pmatrix} 1 & 0 \\ 0 & 1/r^2 \end{pmatrix} = a^{\alpha\beta}. \tag{S17}$$

From Equation S16 we can further write term I as

$$\begin{aligned} \mathsf{I} &= (W_D \zeta^\alpha \zeta^\beta)_{;\beta\alpha} - \frac{1}{2} \Delta(W_D) \\ &= \eta^\beta_{;\beta} - \frac{1}{2} \Delta(W_D), \end{aligned} \tag{S18}$$

where

$$\begin{aligned} \eta^\beta &= \left(W_D \zeta^\alpha \zeta^\beta \right)_{;\alpha} \\ &= \left(W_D \zeta^\alpha \zeta^\beta \right)_{,\alpha} + W_D \Gamma^\alpha_{\alpha\gamma} \zeta^\gamma \zeta^\beta + W_D \Gamma^\beta_{\alpha\gamma} \zeta^\alpha \zeta^\gamma. \end{aligned} \tag{S19}$$

The components of η^β are estimated below in two principal directions

$$\eta^1 = 0 + 0 + W_D \Gamma^1_{22} \zeta^2 \zeta^2 = -\frac{\cos\psi}{r} W_D, \tag{S20}$$

and

$$\eta^2 = 0 + 0 + 0 = 0. \tag{S21}$$

The divergent $\eta^\beta_{;\beta}$ reduces to

$$\begin{aligned} \eta^\beta_{;\beta} &= \frac{1}{\sqrt{a}} (\sqrt{a} \eta^\beta)_{,\beta} \\ &= \frac{1}{r} (r \eta^1)_{,1} \\ &= -\frac{(\cos\psi W_D)'}{r}. \end{aligned} \tag{S22}$$

Substituting the expression of $\eta^\beta_{;\beta}$ in Equation S16 we get term I simplified as

$$\mathsf{I} = -\frac{1}{2} \Delta(W_D) - \frac{(\cos\psi W_D)'}{r}. \tag{S23}$$

Next, we simplify term II below

$$
\begin{aligned}
\text{II} &= \frac{1}{2} W_D \left(\zeta^\alpha \zeta^\beta - \mu^\alpha \mu^\beta \right) b_{\alpha\gamma} b^\gamma_\beta \\
&= \frac{1}{2} W_D \left\{ \zeta^2 \zeta^2 b_{22} b^2_2 - \mu^1 \mu^1 b_{11} b^1_1 \right\} \\
&= \frac{1}{2} W_D \left\{ \frac{\sin^2 \psi}{r^2} - \psi'^2 \right\} \\
&= \frac{1}{2} W_D \left(\frac{\sin \psi}{r} + \psi' \right) \left(\frac{\sin \psi}{r} - \psi' \right) \\
&= \frac{1}{2} W_D \; 2H \; 2D \\
&= 2HDW_D.
\end{aligned}
\tag{S24}
$$

Finally, using the simplifications of term I (Equation (S23)) and term II (Equation (S24)), the shape equation becomes

$$
p = \frac{L'}{r} + W_H \left(2H^2 - K \right) - 2H \left(W + \lambda - W_D D \right), \tag{S25}
$$

where L relates to the expression of the traction as shown in Equation (S10), given by

$$
L/r = \frac{1}{2} \left[(W_H)' - (W_D)' \right] - \frac{\cos \psi}{r} W_D = -F_n. \tag{S26}
$$

The above relation gives a natural boundary condition for L at the center and the boundary. At the center it directly correlates with the value of pulling force as

$$
p_f = \lim_{r \longrightarrow 0} 2\pi r F_n = -2\pi L(0). \tag{S27}
$$

Note than the derivation of shape equation was presented in (*26*) where the last term was missing in the definition of L/r in Equation (S26) and which led to an incorrect residual term $\frac{(W_D)' \cos \psi}{r}$ in the shape equation. Please note that an artificial pulling force was introduced for the boundary condition of $L = 0$ at the center of the membrane with the incomplete expression as presented in Walani et al. (*26*).

B.2 Area parameterization

The governing equation is solved on a patch of membrane with fixed surface area, where the coat area of protein is prescribed. The arclength parametrization poses some difficulty since total arclength varies depending on the equilibrium shape of the membrane. Therefore, we did a coordinate transformation of arclength to a local area a as given by

$$
\frac{\partial}{\partial s} = 2\pi r \frac{\partial}{\partial a}. \tag{S28}
$$

Note that in the differential form local area relates as

$$
da = 2\pi r ds \tag{S29}
$$

The tangential force balance relation in Equation 7 transforms to

$$
\frac{\partial \lambda}{\partial a} = 2\kappa (H - C_0) \frac{\partial C_0}{\partial a} + 2\kappa_d (D - D_0) \frac{\partial D_0}{\partial a}. \tag{S30}
$$

The normal force balance relation in Equation 8 becomes

$$
p = 2\pi \frac{\partial L}{\partial a} + 2\kappa (H - C_0) \left(2H^2 - K \right) - 2H \left(W + \lambda - 2\kappa_d D (D - D_0) \right) \tag{S31}
$$

where,

$$
\frac{L}{r} = \pi r \frac{\partial}{\partial a} \left\{ \kappa (H - C_0) - \kappa_d (D - D_0) \right\} - 2\kappa_D (D - D_0) \frac{\cos \psi}{r}. \tag{S32}
$$

B.3 Non-dimensionalization

In this section we use $(\tilde{\cdot})$ to represent the dimensionless quantities. We used a scale of curvature $1/R_0$, where R_0 is the equivalent lengthscale in the domain. The dimensionless mean, deviatoric and Gaussian curvature becomes $\tilde{H} = R_0 H$, $\tilde{D} = R_0 D$, and $\tilde{K} = R_0^2 K$. The same scale for curvature is used to nondimensionalize spontaneous mean and deviatoric curvatures and they become $\tilde{C}_0 = R_0 C_0$ and $\tilde{D}_0 = R_0 D_0$. The area is dimensionalized with scale $A_0 = 2\pi R_0^2$. The scale for membrane tension is taken as κ/R_0^2, therefore $\tilde{\lambda} = R_0^2\lambda/\kappa$. The dimensionless form of L becomes $\tilde{L} = R_0 L/\kappa$.
The tangential force balance relation in Equation (S30) reads as

$$\frac{\partial\tilde{\lambda}}{\partial\tilde{a}} = 2(\tilde{H}-\tilde{C}_0)\frac{\partial\tilde{C}_0}{\partial\tilde{a}} + 2\tilde{\kappa}_d(\tilde{D}-\tilde{D}_0)\frac{\partial\tilde{D}_0}{\partial\tilde{a}}, \tag{S33}$$

where $\tilde{\kappa}_d = \frac{\kappa_d}{\kappa}$ represents the dimensionless deviatoric curvature. The normal force balance relation in Equation (S31) simplifies to

$$\begin{aligned}\tilde{p} = \frac{\partial\tilde{L}}{\partial\tilde{a}} + 2(\tilde{H}-\tilde{C}_0)\left(2\tilde{H}^2-\tilde{K}\right) - 2\tilde{H}\Big\{&(\tilde{H}-\tilde{C}_0)^2 + \tilde{\kappa}_d(\tilde{D}-\tilde{D}_0)^2 \\ &+ \tilde{\lambda} - 2\tilde{\kappa}_d\tilde{D}(\tilde{D}-\tilde{D}_0)\Big\},\end{aligned} \tag{S34}$$

with

$$\frac{\tilde{L}}{\tilde{r}} = \tilde{r}^2\frac{\partial}{\partial\tilde{a}}\Big\{(H-C_0) - \tilde{\kappa}_d(D-D_0)\Big\} - 2\tilde{\kappa}_d(D-D_0)\frac{\cos\psi}{r}. \tag{S35}$$

C Supplementary Figures

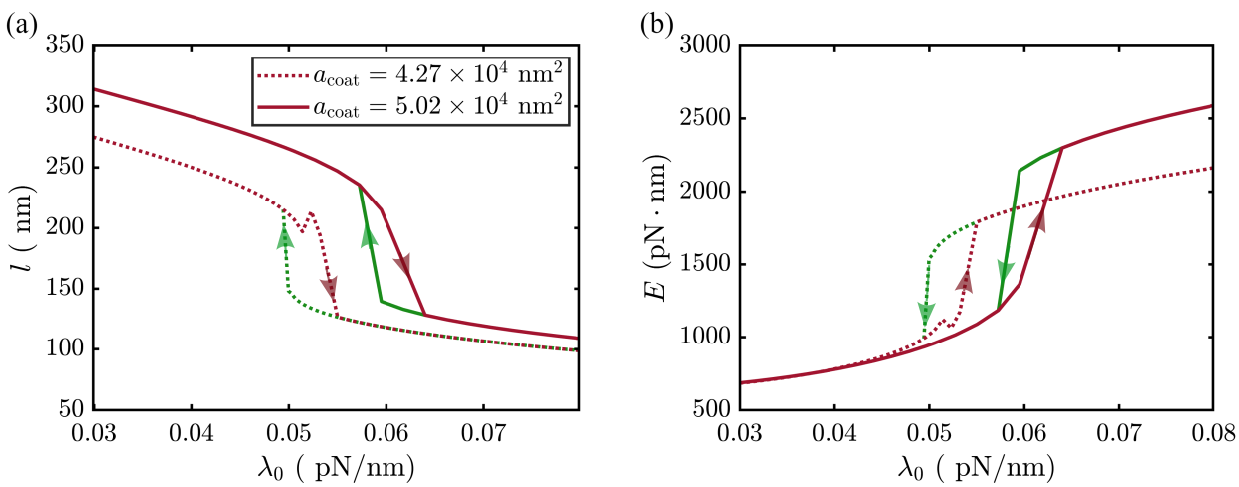

Figure S2: Forward and backward transition to demonstrate snapthrough instability. (a) Transition of tube length in the direction of increasing and decreasing membrane tension for $D_0 = 0.017$ nm^{-1} and $\kappa = 168$ pN · nm and two different values of coat area of proteins. (b) Transition of bending energy in the direction of increasing and decreasing membrane tension for $D_0 = 0.017$ nm^{-1} and $\kappa = 168$ pN · nm and two different values of coat area of proteins.

References

1. A. Mahapatra, C. Uysalel, P. Rangamani, The mechanics and thermodynamics of tubule formation in biological membranes. *The Journal of membrane biology* **254**, 273–291 (2021).
2. F. Yuan *et al.*, Membrane bending by protein phase separation. *Proc. Natl. Acad. Sci. USA* **118** (Mar. 2021).
3. H. Alimohamadi, P. Rangamani, Modeling membrane curvature generation due to membrane– protein interactions. *Biomolecules* **8**, 120–147 (2018).

4. I. Derényi, F. Jülicher, J. Prost, Formation and interaction of membrane tubes. *Physical review letters* **88**, 238101 (2002).
5. A. Roux *et al.*, A minimal system allowing tubulation with molecular motors pulling on giant liposomes. *Proceedings of the National Academy of Sciences* **99**, 5394–5399 (2002).
6. T. Hong *et al.*, Cardiac BIN1 folds T-tubule membrane, controlling ion flux and limiting arrhythmia. *Nature medicine* **20**, 624–632 (2014).
7. R. Rabl *et al.*, Formation of cristae and crista junctions in mitochondria depends on antagonism between Fcj1 and Su e/g. *Journal of Cell Biology* **185**, 1047–1063 (2009).
8. M. Simunovic, G. A. Voth, A. Callan-Jones, P. Bassereau, When physics takes over: BAR proteins and membrane curvature. *Trends in cell biology* **25**, 780–792 (2015).
9. T. Hong, R. M. Shaw, Cardiac T-Tubule Microanatomy and Function. *Physiological Reviews* **97**, 227–252 (2017).
10. H. Mollenhauer, D. J. Morré, The tubular network of the Golgi apparatus. *Histochemistry and cell biology* **109**, 533–543 (1998).
11. I. Raote *et al.*, TANGO1 membrane helices create a lipid diffusion barrier at curved membranes. *Elife* **9**, e57822 (2020).
12. K. Farsad *et al.*, Generation of high curvature membranes mediated by direct endophilin bilayer interactions. *J. Cell Biol.* **155**, 193–200 (2001).
13. K. Takei, P. S. McPherson, S. L. Schmid, P. De Camilli, Tubular membrane invaginations coated by dynamin rings are induced by GTP-γS in nerve terminals. *Nature* **374**, 186–190 (1995).
14. K. Takei *et al.*, Generation of coated intermediates of clathrin-mediated endocytosis on protein-free liposomes. *Cell* **94**, 131–141 (1998).
15. K. Takei, V. I. Slepnev, V. Haucke, P. De Camilli, Functional partnership between amphiphysin and dynamin in clathrin-mediated endocytosis. *Nature cell biology* **1**, 33–39 (1999).
16. J. C. Stachowiak, C. C. Hayden, D. Y. Saski, Steric confinement of proteins on lipid membranes can drive curvature and tubulation. *Proc. Natl. Acad. Sci.* **107**, 7781–7786 (2010).
17. A. Arkhipov, Y. Yin, K. Schulten, Membrane-bending mechanism of amphiphysin N-BAR domains. *Biophysical journal* **97**, 2727–2735 (2009).
18. Y. Yin, A. Arkhipov, K. Schulten, Simulations of membrane tubulation by lattices of amphiphysin N-BAR domains. *Structure* **17**, 882–892 (2009).
19. H. Noguchi, C. Tozzi, M. Arroyo, Binding of anisotropic curvature-inducing proteins onto membrane tubes. *Soft Matter* **18**, 3384–3394 (2022).
20. W. Helfrich, Elastic Properties of Lipid Bilayers: Theory and Possible experiments. *Z. Naturforsch. C* **5**, 693–703 (1973).
21. H. Naito, M. Okuda, O.-Y. Zhong-Can, New solutions to the Helfrich variation problem for the shapes of lipid bilayer vesicles: beyond Delaunay's surfaces. *Physical review letters* **74**, 4345 (1995).
22. P. Rangamani, A. Behzadan, M. Holst, Local sensitivity analysis of the "membrane shape equation" derived from the Helfrich energy. *Math. Mech. Sol.* **26**, 356–385 (2021).
23. A. Iglič, B. Babnik, U. Gimsa, V. Kralj-Iglič, On the role of membrane anisotropy in the beading transition of undulated tubular membrane structures. *J. Phys. A* **40**, 8527–8536 (2005).
24. A. Iglič *et al.*, Possible role of flexible red blood cell membrane nanodomains in the growth and stability of membrane nanotubes. *Blood Cells, Molecules, and Diseases* **39**, 14–23 (2007).
25. N. Bobrovska, W. Gozdz, V. Kralj-Iglic, A. Iglic, On the Role of Anisotropy of Membrane Components in Formation and Stabilization of Tubular Structures in Multicomponent Membranes. *PLOS ONE* **8**, e73941 (2013).
26. N. Walani, J. Torres, A. Agrawal, Anisotropic spontaneous curvatures in lipid membranes. *Phys. Rev. E* **89**, 062715 (2014).
27. N. Walani, J. Torres, A. Agrawal, Endocytic proteins drive vesicle growth via instability in high membrane tension environment. *Proceedings of the national academy of sciences* **112**, E1423–E1432 (2015).
28. K. Murayama, M. Kato-Murayama, T. Terada, M. Shirouzu, S. Yokoyama, Crystal structure of BAR domain of Endophilin-III. *RIKEN Structural Genomics Proteomics Initiative (RSGI)*, DOI `10.2210/pdb2Z0V/pdb` (2008).

29. M. B. Schneider, J. Jenkins, W. Webb, Thermal fluctuations of large quasi-spherical bimolecular phospholipid vesicles. *J. Phys. (Paris),* **45**, 1457–1472 (1984).
30. P. W. Fowler *et al.*, Membrane stiffness is modified by integral membrane proteins. *Soft Matter* **12**, 7792–7803 (2016).
31. R. Lipowsky, Spontaneous tubulation of membranes and vesicles reveals membrane tension generated by spontaneous curvature. *Faraday Discuss.* **161**, 305–331 (2013).
32. P. Rangamani, The many faces of membrane tension: Challenges across systems and scales. *Biochimica et Biophysica Acta (BBA)-Biomembranes* **1864**, 183897 (2022).
33. J. E. Hassinger, G. Osterb, D. G. Drubinb, P. Rangamani, Design principles for robust vesiculation in clathrin-mediated endocytosis. *Proc. Natl. Acad. Sci.* **114**, 1118–1127 (2017).
34. V. Kralj-Iglič *et al.*, Amphiphile-induced tubular budding of the bilayer membrane. *Eur. Biophys. J.* **34**, 1066–1070 (2005).
35. D. Kabaso *et al.*, Attachment of rod-like (BAR) proteins and membrane shape. *Mini Rev. Med. Chem.* **11**, 272–282 (2011).
36. S. Perutkova, V. Kralji-Iglic, M. Frank, A. Iglic, Mechanical stability of membrane nanotubular protrusion influenced by attachment of flexible rod-like protein. *J. Biomech.* **43**, 1612–1617 (2010).
37. C. Tozzi, N. Walani, A.-L. Le Roux, P. Roca-Cusachs, M. Arroyo, A theory of ordering of elongated and curved proteins on membranes driven by density and curvature. *Soft matter* **17**, 3367–3379 (2021).
38. D. J. Steigmann, Fluid films with curvature elasticity. *Arch. Rat. Mech.* **150**, 257–272 (1999).
39. D. Steigmann, E. Baesu, R. E. Rudd, J. Belak, M. McEleresh, On the variational theory of cell-membrane equilibria. *Interfaces Free Bound.* **5**, 357–366 (2003).
40. P. Rangamani, A. Agrawal, K. Mandadapu, G. Oster, D. Steigmann, Interaction between surface shape and intra-surface viscous flow on lipid membranes. *Biomech. Model. Mechanobiol.* **12**, 833–845 (2013).
41. P. Rangamani, K. Mandadapu, G. Oster, Protein induced membrane curvature alters local membrane tension. *Biophys. J.* **107**, 751–762 (2014).
42. A. Mahapatra, D. Saintillan, P. Rangamani, Transport phenomena in fluid films with curvature elasticity. *J. Fluid Mech.* **905**, 1–31 (2020).
43. A. Mahapatra, D. Saintillan, P. Rangamani, Curvature-driven feedback on aggregation–diffusion of proteins in lipid bilayers. *Soft Matter* **17**, 8373–8386 (2021).
44. Y. F. Barooji, A. Rørvig-Lund, S. Semsey, S. N. S. Reihani, P. M. Bendix, Dynamics of membrane nanotubes coated with I-BAR. *Scientific reports* **6**, 1–12 (2016).
45. M. Gomez, D. E. Moulton, D. Vella, Critical slowing down in purely elastic 'snap-through'instabilities. *Nature Physics* **13**, 142–145 (2017).
46. B. L. Goode, J. A. Eskin, B. Wendland, Actin and endocytosis in budding yeast. *Genetics* **199**, 315–358 (2015).
47. J. Liu, Y. Sun, D. G. Drubin, G. F. Oster, The mechanochemistry of endocytosis. en, *PLoS Biol.* **7**, e1000204 (Sept. 2009).
48. M. Kaksonen, C. P. Toret, D. G. Drubin, A modular design for the clathrin-and actin-mediated endocytosis machinery. *Cell* **123**, 305–320 (2005).
49. E. Sitarska, A. Diz-Muñoz, Pay attention to membrane tension: Mechanobiology of the cell surface. *Current opinion in cell biology* **66**, 11–18 (2020).
50. Z. Shi, Z. T. Graber, T. Baumgart, H. A. Stone, A. E. Cohen, Cell Membranes Resist Flow. en, *Cell* **175**, 1769–1779.e13 (Dec. 2018).
51. E. Lee *et al.*, Amphiphysin 2 (Bin1) and T-tubule biogenesis in muscle. *Science* **297**, 1193–1196 (2002).
52. C. Anselmi, K. M. Davies, J. D. Faraldo-Gómez, Mitochondrial ATP synthase dimers spontaneously associate due to a long-range membrane-induced force. en, *J. Gen. Physiol.* jgp.201812033 (Apr. 2018).
53. K. M. Davies *et al.*, Macromolecular organization of ATP synthase and complex I in whole mitochondria. en, *Proc. Natl. Acad. Sci. U. S. A.* **108**, 14121–14126 (Aug. 2011).
54. I. Raote *et al.*, A physical mechanism of TANGO1-mediated bulky cargo export. en, *Elife* **9** (Nov. 2020).
55. G. Vitale *et al.*, T-tubule remodeling in human hypertrophic cardiomyopathy. *Journal of Muscle Research and Cell Motility* **42**, 305–322 (2021).
56. K. Zhou, T. Hong, Cardiac BIN1 (cBIN1) is a regulator of cardiac contractile function and an emerging biomarker of heart muscle health. *Science China Life Sciences* **60**, 257–263 (2017).

57. T. Kishimoto *et al.*, Determinants of endocytic membrane geometry, stability, and scission. *Proceedings of the National Academy of Sciences* **108**, E979–E988 (2011).
58. R. T. Sutton, O. R. Zaiane, R. Goebel, D. C. Baumgart, Artificial intelligence enabled automated diagnosis and grading of ulcerative colitis endoscopy images. *Scientific Reports* **12**, 1–10 (2022).
59. B. R. Capraro, Y. Yoon, W. Cho, T. Baumgart, Curvature sensing by the epsin N-terminal homology domain measured on cylindrical lipid membrane tethers. *Journal of the American Chemical Society* **132**, 1200–1201 (2010).
60. T. Baumgart, B. R. Capraro, C. Zhu, S. L. Das, Thermodynamics and mechanics of membrane curvature generation and sensing by Proteins and Lipids. *Annu. Rev. Phys. Chem.* **62**, 483–506 (2011).
61. A. Frost *et al.*, Structural basis of membrane invagination by F-BAR domains. *Cell* **132**, 807–817 (2008).
62. M. Akamatsu *et al.*, Principles of self-organization and load adaptation by the actin cytoskeleton during clathrin-mediated endocytosis. *Elife* **9**, e49840 (2020).
63. D. Serwas *et al.*, Mechanistic insights into actin force generation during vesicle formation from cryo-electron tomography. *Developmental cell* **57**, 1132–1145 (2022).
64. M. Abella, L. Andruck, G. Malengo, M. Skruzny, Actin-generated force applied during endocytosis measured by Sla2-based FRET tension sensors. *Developmental Cell* **56**, 2419–2426 (2021).
65. R. Vasan, S. Rudraraju, M. Akamatsu, K. Garikipati, P. Rangamani, A mechanical model reveals that non-axisymmetric buckling lowers the energy barrier associated with membrane neck constriction. *Soft Matter* **16**, 784–797 (2020).
66. C. Zhu, C. T. Lee, P. Rangamani, Mem3DG: modeling membrane mechanochemical dynamics in 3D using discrete differential geometry. *Biophysical Journal* **121**, 71a (2022).
67. D. Auddya *et al.*, Biomembranes undergo complex, non-axisymmetric deformations governed by Kirchhoff-Love kinematics and revealed by a three dimensional computational framework. *arXiv preprint arXiv:2101.11929* (2021).
68. A. Agrawal, D. J. Steigmann, Boundary-value problems in the theory of lipid membranes. *Continuum Mech. Therm.* **21**, 57–82 (2009).